INORGANIC CHEMISTRY
FRONTIERS

RESEARCH ARTICLE

View Article Online
View Journal | View Issue

Cite this: *Inorg. Chem. Front.*, 2025, **12**, 7068

Conjugation of a cyclometalated Ir(III) complex to human serum albumin for oncosis-mediated photodynamic therapy

Antonio Linero-Artiaga,[a,b,c] Lisa-Marie Servos,[a] Zisis Papadopoulos,[a] Venancio Rodríguez,[b,c] José Ruiz *[b,c] and Johannes Karges *[a]

Anticancer agents often rely on apoptosis, limiting their effectiveness and leading to drug resistance. To address these issues, alternative cell death mechanisms have gained attention. To date, only very few metal complexes that trigger oncosis have been reported. Herein, the conjugation of a cyclometalated Ir (III) complex to human serum albumin for oncosis mediated photodynamic therapy is reported. While being non-toxic in the dark, the conjugate showed strong therapeutic effects upon irradiation in cancer cells and tumor spheroids. Biological mechanistic analyses revealed that the conjugate preferentially accumulated in mitochondria, induced NADH oxidation, caused oxidative damage to the cell membrane, depleted ATP, and triggered Ca^{2+} influx, inducing cellular swelling and vacuolization of the cytoplasm as well as the formation of organelle-free blisters, ultimately leading to cell death by oncosis. This work presents the first example of a photo-responsive metal complex human serum albumin conjugate that induces oncosis.

Received 10th June 2025,
Accepted 23rd July 2025

DOI: 10.1039/d5qi01287b

rsc.li/frontiers-inorganic

Introduction

Photodynamic therapy (PDT) is a clinically approved medical technique for the treatment of cancer (*i.e.*, bladder, lung, brain, or esophageal cancers) as well as bacterial, viral, and, fungal infections. In PDT, a photosensitizer is locally or systemically administrated at a non-toxic dose. After a specified incubation time, the targeted tumorous tissue is irradiated with light. When the photosensitizer is exposed to light, it is first excited to a higher energy singlet state, before transitioning to a triplet state through intersystem crossing. In this triplet state, the photosensitizer can induce the production of reactive oxygen species (ROS) through two primary mechanisms. The type I pathway involves the photosensitizer transferring electrons to adjacent molecules, leading to the formation of reactive radicals like superoxide or hydroxyl radicals. In the type II pathway, the photosensitizer transfers energy to molecular oxygen (O_2), generating singlet oxygen ($^1O_2$). The majority of photosensitizers primarily function through the type II mechanism when interacting with biological systems.[1–5] Among the most promising types of photosensitizers, cyclometalated Ir(III) complexes are gaining much interest due to their attractive photophysical and biological properties (*i.e.*, strong emission, large Stokes shift, ROS generation, biocompatibility).[6–12] Despite these promising characteristics, Ir(III) complexes often display low aqueous solubility due to their high lipophilicity, limiting their application in PDT.[13–16] To overcome this challenge, the conjugation of metallodrugs to human serum albumin (HSA) has recently been explored to enhance their solubility and cellular uptake of drug candidates.[17–24] HSA is the most prevalent extracellular protein in plasma, essential for regulating blood colloidal osmotic pressure, stabilizing pH, and transporting various metabolites such as fatty acids, hormones, and bilirubin from the bloodstream to cells. Its unique three-dimensional structure makes it highly efficient for drug delivery.[25,26] The palladium(II) bacteriochlorophyll derivative WST11 (TOOKAD® soluble), that has been clinically approved as a photosensitizer for PDT, has been reported to preferentially bind non-covalently to HSA during circulation, leading to high accumulation in the prostate and therefore an efficient drug delivery.[27,28] Despite the growing interest in albumin-bound photosensitizers, most reported systems exhibit only weak to moderate affinity for the protein. Moreover, the underlying mechanisms governing the interactions between photosensitizers and albumin remain largely unexplored, resulting in a critical gap in our understanding of how non-covalent forces can be harnessed to enhance metal–albumin binding.

[a]*Faculty of Chemistry and Biochemistry, Ruhr-University Bochum, Universitätstrasse 150, 44780 Bochum, Germany. E-mail: johannes.karges@ruhr-uni-bochum.de*
[b]*Departamento de Química Inorgánica, Universidad de Murcia, Campus de Espinardo, 30100 Murcia, Spain*
[c]*Institute for Bio-Health Research of Murcia (IMIB-Arrixaca), Murcia, Spain. E-mail: jruiz@um.es*

To address this limitation, we recently developed an Ir(III) photosensitizer with markedly improved affinity for albumin. Guided by theoretical calculations, we found that the strategic incorporation of thiophenyl moieties, fluorinated substituents, and ester groups on the cyclometalated Ir(III) scaffold collectively enhanced hydrophobic, electrostatic, and hydrogen-bonding interactions with the protein.[22]

Despite recent research progress in PDT, most of photosensitizers trigger cell death by apoptosis and are therefore prone to the development of drug resistances.[4,29] Capitalizing on this, there is a high demand in photosensitizers that induce cell death by non-apoptotic cell death mechanisms.[13,29–32] Among the clinically most promising cell death mechanism, the induction of cell death by oncosis is receiving much interest. Oncosis is a form of programmed cell death characterized by cellular swelling, chromatin clumping, cytosol clearing, and increased membrane permeability. It involves mitochondrial dysfunction due to early opening of permeability transition pores, leading to depolarization, ROS production, ATP depletion, and ion pump failure. This disruption causes water influx, organelle-free blister formation, and ultimately, membrane rupture.[33–37] Although several molecular organic agents have been identified as inducers of oncosis,[37] metal complexes capable of triggering oncosis remain highly rare (see Fig. S1 for an overview of previously reported oncosis-inducing metal complexes of relevance).[38–42] Moreover, to the best of our knowledge, there are no reports on photosensitizer-HSA conjugates that trigger oncosis. For all these reasons, the chemical synthesis and biological evaluation of the conjugation of a cyclometalated Ir(III) (**Onc1**) as a photosensitizer with HSA (**Onc1@HSA**) for oncosis mediated PDT is reported. While being non-toxic in the dark, **Onc1@HSA** was found to photocatalytically oxidize NADH and generate singlet oxygen upon light irradiation, causing a cytotoxic response against murine colon cancer cells and multicellular tumor spheroids in the very low micromolar range. Further analyses demonstrated that **Onc1@HSA** preferentially accumulated in mitochondria, induced NADH oxidation, triggered oxidative damage to the cell membrane, depleted ATP, and triggered Ca^{2+} influx, inducing cellular swelling and vacuolization of the cytoplasm as well as the formation of organelle-free blisters, ultimately leading to cell death by oncosis (Fig. 1). This study reports on the first example of a photo-responsive metal complex–HSA conjugate capable of inducing oncosis.

Results and discussion

Synthesis and characterization

2-Thienylcarboxaldehyde and 3,4-difluoro-1,2-phenylenediamine were condensed to yield 5,6-difluoro-2-(thiophen-2-yl)-1*H*-benzo[*d*]imidazole. This intermediate was further reacted with 4-(trifluoromethyl)benzyl bromide to obtain the cyclometalated ligand 5,6-difluoro-2-(thiophen-2-yl)-1-(4-(trifluoromethyl)benzyl)-1*H*-benzo[*d*]imidazole. The compound was then suspended with iridium trichloride in a mixture of 2-ethoxyethanol/water and heated at reflux, leading to the formation of the dimeric complex [Ir(5,6-difluoro-2-(thiophen-2-yl)-1-(4-(trifluoromethyl)benzyl)-1*H*-benzo[*d*]imidazole)$_2$(μ-Cl)]$_2$. The dimeric metal precursor and the ancillary ligand 2-(pyridin-2-yl)-1*H*-benzo[*d*]imidazole were dissolved in a dichloromethane/methanol mixture and heated overnight to

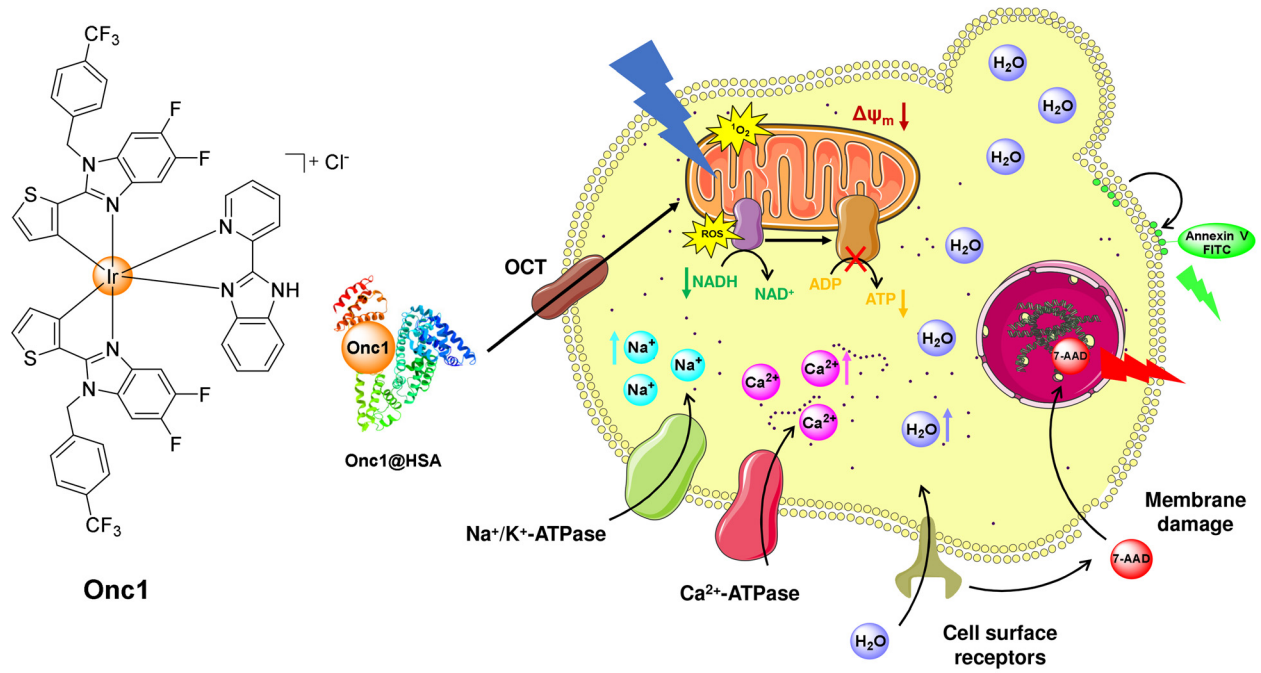

Fig. 1 Chemical structure of complex **Onc1** and overview of biological mechanism of action of **Onc1@HSA** by oncosis-mediated PDT.

obtain the desired compound [Ir(5,6-difluoro-2-(thiophen-2-yl)-1-(4-(trifluoromethyl)benzyl)-1*H*-benzo[*d*]imidazole)$_2$ (2-(pyridin-2-yl)-1*H*-benzo[*d*]imidazole)][Cl] (**Onc1**) (synthetic strategy: Scheme S1).

The identity of the compounds was confirmed using ^{1}H-, ^{13}C- and ^{19}F{^{1}H}-NMR spectroscopy (Fig. S2–S11) as well as high-resolution electron spray ionization mass spectrometry (Fig. S12). Proton and carbon signals were further assigned by 2D ^{1}H–^{1}H COSY, ^{1}H–^{1}H NOESY, ^{1}H–^{13}C HSQC, and ^{1}H–^{13}C HMBC spectra. The proton signals were assigned using the Nuclear Overhauser Effect observed in interligand H^{A}–$H^{7}/H^{7'}$, H^{H}–$H^{7}/H^{7'}$ and H^{H}–$H^{2}/H^{2'}$ and intraligand $H^{10+10'}$–$H^{12+12'}$ cross peaks (Fig. S8–S11). The results showed a double signal set of peaks associated with an asymmetric ligand environment of the metal complex. The purity of the complex was verified by high performance liquid chromatography and elemental analysis (Fig. S13).

Photophysical properties and DFT calculations

The photophysical properties of the iridium(III) metal complex were systematically investigated to evaluate its potential as a photosensitizer for PDT. The absorption spectrum of the complex was recorded in water and the corresponding absorption bands were assigned based on density functional theory (DFT) calculations. The complex exhibited intense absorption bands in the 310–320 nm region, which were attributed to ligand-centered $\pi \rightarrow \pi^*$ transitions originating from both the cyclometalated and ancillary ligands. Additionally, weaker absorption bands of **Onc1** were observed in the 410–430 nm range, primarily associated with metal-to-ligand charge transfer transitions (Fig. 2a, Fig. S14).[43–45] A bathochromic shift in the metal-to-ligand charge transfer band was observed upon solvent variation from polar water to apolar acetonitrile, indicating the involvement of charge transfer in these transitions.[44,45] The highest occupied molecular orbital (HOMO) was predominantly localized on the d-orbitals of the iridium center and the π-orbitals of the cyclometalated ligands, whereas the lowest unoccupied molecular orbital (LUMO) was primarily composed of π* orbitals from the ancillary ligand (Fig. 2b). Consequently, the HOMO–LUMO gap of **Onc1** encompassed both metal-to-ligand charge transfer ($d_M \rightarrow \pi^*_{N^\wedge N}$) and ligand-to-ligand charge transfer ($\pi_{C^\wedge N} \rightarrow \pi^*_{N^\wedge N}$) transitions, highlighting the complex's charge-transfer characteristics (optimized coordinates: Table S1).

The emission spectra of the iridium(III) complex displayed a broad emission range spanning 500–700 nm (Fig. S15). The emission properties of **Onc1** were analyzed in various solvents, revealing that the more energetic peak remained unaffected by increasing solvent polarity, while the less energetic peak exhibited both a bathochromic and hypochromic shift. These spectral variations led to a subtle emission color change from orange to yellow, suggesting the involvement of dual ligand-centered and metal-to-ligand charge transfer transitions (Fig. S16 and S17).[43] Time-dependent density functional theory (TD-DFT) calculations of singlet and triplet vertical transitions (Fig. 2c) determined an S_0–S_1 gap of 2.58 eV (481 nm) and an S_0–T_1 gap of 2.27 eV (546 nm). Notably, the latter exceeds the energy gap between ground-state oxygen and singlet excited oxygen molecules (0.98 eV),[46] indicating the potential for photocatalytic generation of singlet oxygen by a type II PDT mechanism. Furthermore, the S_1–T_1 gap was calculated to be 0.31 eV, surpassing the threshold (≥0.2 eV) required for efficient and irreversible intersystem crossing.[47] Analysis of the vertical transitions revealed that the excitation of **Onc1** from the ground state to its singlet excited state was primarily governed by HOMO → LUMO transitions, further supporting the presence of metal-to-ligand charge transfer and ligand-to-ligand charge transfer processes in the lowest-lying excited state (Table S2). Emission quantification indicated that **Onc1** exhibited moderate emission, with an emission quantum yield of 4.5%. The emission decay profile followed a biexponential pattern, consisting of a short-lived component (34 ns) with a minor contribution and a dominant long-lived component (156 ns) (overview of photophysical properties: Table S3).

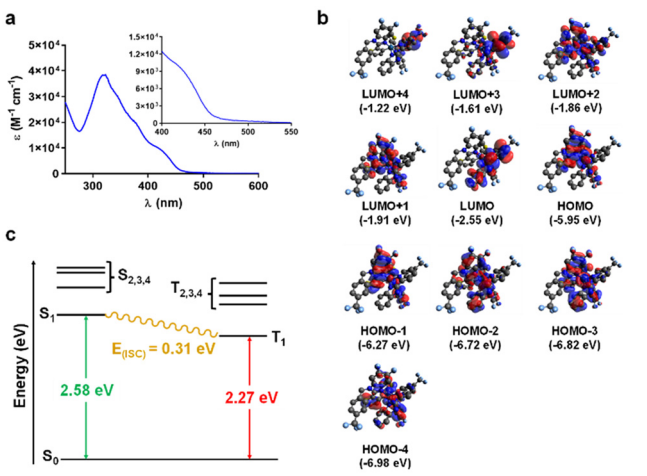

Fig. 2 (a) UV/VIS absorption spectra of complex **Onc1** (10 μM) in a H_2O/DMSO (99 : 1) mixture. (b) Molecular orbitals for complex **Onc1** computed in acetonitrile by DFT calculations using the PBE0 level of theory and 6-31G(d) and LANL2DZ as basis sets. (c) Vertical transitions found for complex **Onc1** with the assistance of (TD)-DFT calculations.

Photo-catalytic production of singlet oxygen and hydroxyl radicals

The catalytic ability of the photosensitizer to generate ROS upon irradiation was then investigated. The energy transfer from the excited state of the metal complex to O_2, leading to the production of $^{1}O_2$, was assessed by capturing $^{1}O_2$ with 1,3-diphenylisobenzofurane and monitoring changes in the absorption spectrum of the probe over irradiation time.[48] No changes in the probe were observed when only DPBF was irradiated (Fig. S18), whereas a significant decrease in absorbance was noted upon incubation with **Onc1** and exposure to irradiation (Fig. 3a). A comparison with the reference photosensitizer, [Ru(2,2′-bipyridine)$_3$](Cl)$_2$ (Fig. S19), revealed that **Onc1** had a singlet oxygen quantum yield of 73% (Fig. S20). As a complementary technique, the generation of ROS was

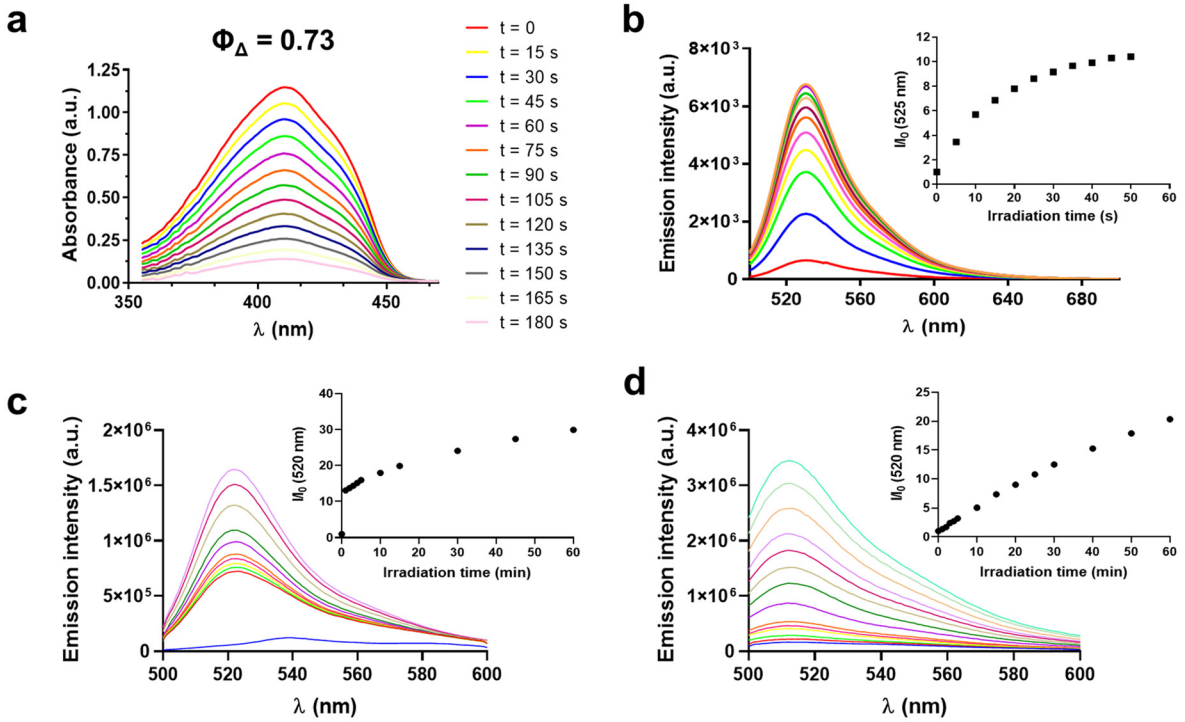

Fig. 3 (a) Changes in the absorption spectrum of 1,3-diphenylisobenzofuran (λ_{abs} = 411 nm, acetonitrile) upon incubation with complex **Onc1** and exposure to blue light irradiation (3 min, λ = 465 nm, 0.5 mW cm^{-2}). (b) Monitoring of the emission spectra of SOSG (1 μM) upon incubation with **Onc1** (6 μM) in a H_2O/DMF (95 : 5) mixture and irradiation with a blue lamp (λ = 450 nm, power: 20%, 50 s, 5 s irradiation intervals). λ_{exc}: 488 nm. (c) Changes in the emission profile of 2′,7′-dichlorodihydrofluorescein diacetate (30 μM) upon incubation with complex **Onc1** (5 μM) in a H_2O/DMF (95 : 5) mixture and exposure to blue light irradiation at short intervals (λ = 465 nm, 5 mW cm^{-2}). λ_{exc}: 490 nm. (d) Monitoring of the emission profile of HPF (10 μM) upon incubation with complex **Onc1** (10 μM) and short blue light irradiation intervals (λ = 465 nm, 5 mW cm^{-2}). λ_{exc}: 490 nm.

assessed by emission spectroscopy using the general ROS probe 2′,7′-dichlorodihydrofluorescein diacetate (H_2DCFDA). Upon light irradiation, a pronounced green fluorescence signal was detected, indicating photoactivation of **Onc1** and the subsequent formation of ROS (Fig. 3c). $^1O_2$ production, indicative of a type II photodynamic mechanism, was further confirmed using the Singlet Oxygen Sensor Green (SOSG) probe. When incubated with the parent complex **Onc1**, a progressive increase in green fluorescence was observed upon periodic light exposure, supporting the generation of $^1O_2$ (Fig. 3b). Notably, control experiments demonstrated that the SOSG probe alone did not undergo significant fluorescence changes upon irradiation (Fig. S21). In addition to type II species, the photoinduced formation of type I ROS was also investigated. Specifically, the generation of hydroxyl radicals ($^{\bullet}$OH)—highly reactive species implicated in the non-selective oxidative damage of cellular components such as DNA, proteins, and lipids[49]—was monitored using the non-fluorescent probe 3′-(*p*-hydroxyphenyl)fluorescein (HPF). Upon incubation with **Onc1** and light irradiation, a marked increase in the emission of the green-fluorescent HPF adduct was observed, indicating efficient $^{\bullet}$OH production (Fig. 3d). No fluorescence increase was observed when HPF was irradiated in the absence of **Onc1** (Fig. S22). Together, these results highlight the dual ROS-generating capacity of **Onc1** and underscore its potential to mediate both type I and type II photodynamic therapeutic pathways.

Photo-catalytic NADH oxidation

Following the study of type I mechanism, the photosensitizer's ability to transfer electrons to adjacent biomolecules was evaluated. **Onc1** was incubated with several relevant biomolecules for cell growth and proliferation (NADH, GSH, Glu, Gly, Pro, Cys, His), followed by irradiation, and qualitatively testing hydrogen peroxide formation with a stripe test. Only the incubation with NADH resulted in a notable discoloration (Fig. 4a), suggesting interaction between **Onc1** and NADH. Nicotinamide adenine dinucleotide hydrogen (NADH) is a coenzyme located in the mitochondrial electron transport chain (ETC) and it has been proven to be crucial for ATP synthesis through the conversion to its oxidized form, NAD^+. Imbalances in the NADH/NAD^+ ratios lead to an impairment in the ETC and the subsequent blockage in ATP synthesis, bereaving cells from their energetic source to proliferate.[50] Time-dependent monitoring of an NADH solution upon incubation with **Onc1** and irradiation revealed a gradual decrease in the absorption band at 339 nm (Fig. 4b), indicating the oxidation of NADH to NAD^+.[50] Quantification of this process determined a turnover frequency for **Onc1** of 6.85 h^{-1}.

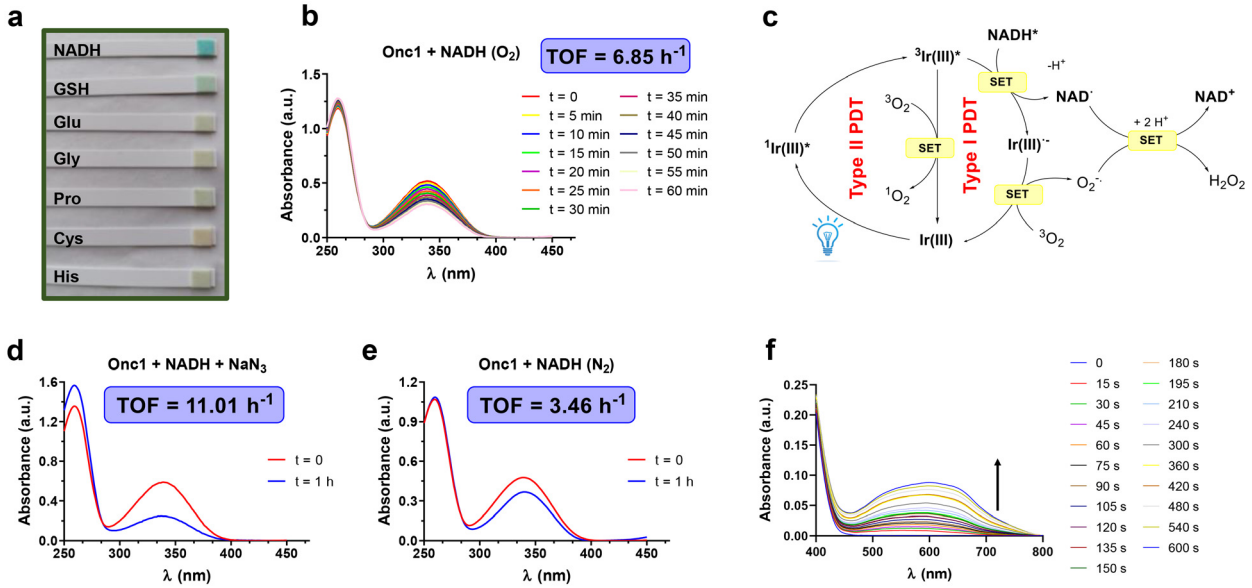

Fig. 4 (a) Hydrogen peroxide stripes dipped into irradiated (1 h, λ = 465 nm, 5 mW cm^{-2}) solutions of biomolecules (1 mM) upon incubation with complex **Onc1** (10 μM). (b) Monitoring of the absorption profile of NADH (100 μM) upon incubation with complex **Onc1** (5 μM) and blue light irradiation (1 h, λ = 465 nm, 5 mW cm^{-2}). (c) Overview of the photo-catalytic oxidative cycle of NADH. Adapted from ref. 7 and 51. Monitoring of the absorption profile of NADH (100 μM) upon coincubation with complex **Onc1** (5 μM) and sodium azide (10 mM) (d) or in deaerated conditions (e) and blue light irradiation (1 h, λ = 465 nm, 5 mW cm^{-2}). (f) Monitoring of the absorption profile of NBT (50 μM) upon incubation with complex **Onc1** (5 μM) and NADH (100 μM) and blue light irradiation (λ = 465 nm, 5 mW cm^{-2}) at short intervals.

No evident changes were detected when NADH was incubated with **Onc1** in the dark (Fig. S23).

To gain deeper insight into the mechanism underlying NADH photooxidation, additional spectroscopic studies were conducted. Based on previous reports on the photocatalytic oxidation of NADH,[7,51] the process is proposed to proceed by a single electron transfer (SET) from NADH to the photosensitizer in its triplet excited state (Fig. 4c). To probe the involvement of triplet excitons, we monitored the time-dependent absorption profile of NADH in the presence of **Onc1** under irradiation, both with and without sodium azide, a well-established singlet oxygen scavenger and inhibitor of type II photoreactions. Interestingly, the turnover frequency (TOF) increased upon the addition of sodium azide (Fig. 4d), suggesting that suppression of the type II pathway redirects the excited-state complex toward a SET-driven, type I photocatalytic mechanism. This observation underscores the competitive interplay between type I and type II pathways in the catalytic cycle. Interestingly, the catalytical ability of **Onc1** to oxidize NADH upon irradiation was partially but not totally inhibited in the absence of oxygen (Fig. 4e), emphasizing its suitability for photoredox therapy under oxygen-deficient conditions.

Following the initial SET event, the resulting reduced photosensitizer radicals react rapidly with molecular oxygen, returning to the ground state and generating superoxide anions ($O_2^{\bullet-}$). These anions can subsequently undergo a second SET with NAD$^{\bullet}$ intermediates to yield oxidized NAD$^+$ and hydrogen peroxide. To confirm the formation of superoxide as part of this mechanism, UV-Vis absorption spectroscopy was performed using nitroblue tetrazolium, a selective superoxide scavenger that produces the blue-colored formazan dye (λ_{abs} = 590 nm) upon reduction. A significant increase in absorbance was observed upon irradiation of **Onc1** in the presence of NADH (Fig. 4f), whereas no such change occurred in the absence of NADH (Fig. S24). These findings strongly support the involvement of superoxide in the catalytic cycle of NADH photooxidation and further validate the type I mechanism facilitated by the triplet state of the photosensitizer.

Stability in solution

As a critical factor for biological applications, the stability of the metal complex was investigated. The compound was dissolved in deuterated DMSO and ^{1}H-NMR spectroscopy was employed to monitor any potential changes. No significant alterations were observed (Fig. S25), indicating that the complex remains stable in dimethyl sulfoxide. The stability of **Onc1** was subsequently evaluated in aqueous solutions and cell culture media using high-performance liquid chromatography coupled with mass spectrometry. No significant changes were detected, suggesting **Onc1** high stability in aqueous solutions (Fig. S26–S28). Followingly, the photostability of the metal complex was evaluated. No significant changes in the spectra were observed, indicative of the high stability of **Onc1** upon irradiation (Fig. S29). Despite these promising properties, the use of moderate concentrations of **Onc1** led to the formation of precipitates. Absorption spectroscopy (Fig. S30), transmission electron microscopy (Fig. S31), and dynamic light scattering (Fig. S32) measurements revealed that particles

began to form even with equivolumetric water–DMSO solutions.

Interaction with human serum albumin (HSA)

To address this severe pharmacological limitation, the physical encapsulation of **Onc1** with HSA is herein proposed. To study the interaction of both compounds, the absorption spectra of HSA upon the addition of **Onc1** was measured. The spectra showed that the more energetic band had a hypochromic and bathochromic shift whereas the less energetic band underwent a slight hypochromic shift (Fig. 5a), indicative of strong binding of **Onc1** to HSA.[22,52] To quantify the binding affinity, a fluorometric titration experiment upon dropwise addition of **Onc1** to a solution of HSA was performed. The intrinsic fluorescence of albumin, primarily originating from tryptophan residues, underwent significant quenching with successive additions of **Onc1** (Fig. 5b), indicating continuous binding of the metal complex to the protein. Maximal changes were observed after addition of one equivalent of **Onc1**, suggestive of the preferential binding in a 1 : 1 ratio. Further analysis of the data revealed an excellent fit to a static quenching process rather than a dynamic quenching process (Fig. S33).[22,52] Scatchard analysis determined a binding constant of 1.04×10^7 M^{-1} of **Onc1** to HSA (Fig. S34). Followingly, the binding site was investigated by preformation of binder–HSA conjugates that block specific binding sites, the addition of **Onc1**, and assess binding of the Ir(III) complex by emission spectroscopy. As specific binding site blockers, warfarin (K_b = 1.63 × 10^5 M^{-1})[53] was used for binding site I and dansyl glycine (K_b = 8.70 × 10^4 M^{-1})[54] for binding site II. The emission intensity of the warfarin–HSA adduct revealed a slight quenching as the concentration of **Onc1** increased (Fig. 5c), suggesting that the metal complex interacts with surface aromatic amino acids of HSA without significantly displacing warfarin from site I. In contrast, the addition of **Onc1** to the dansyl glycine–HSA adduct resulted in a significant decrease in the emission band (Fig. 5d), indicating effective displacement of dansyl glycine from site II. These spectrophotometric findings are further supported by the analysis of emission quenching constants for the warfarin–HSA and dansyl glycine–HSA adducts (Fig. S35, overview of experimental binding parameters: Table S4). To validate the binding site of **Onc1** with HSA, its interaction with the protein was theoretically assessed using molecular docking simulations performed with the Molegro Virtual Docking software. When docking was conducted without spatial constraints, preferential binding of **Onc1** to site II was observed,

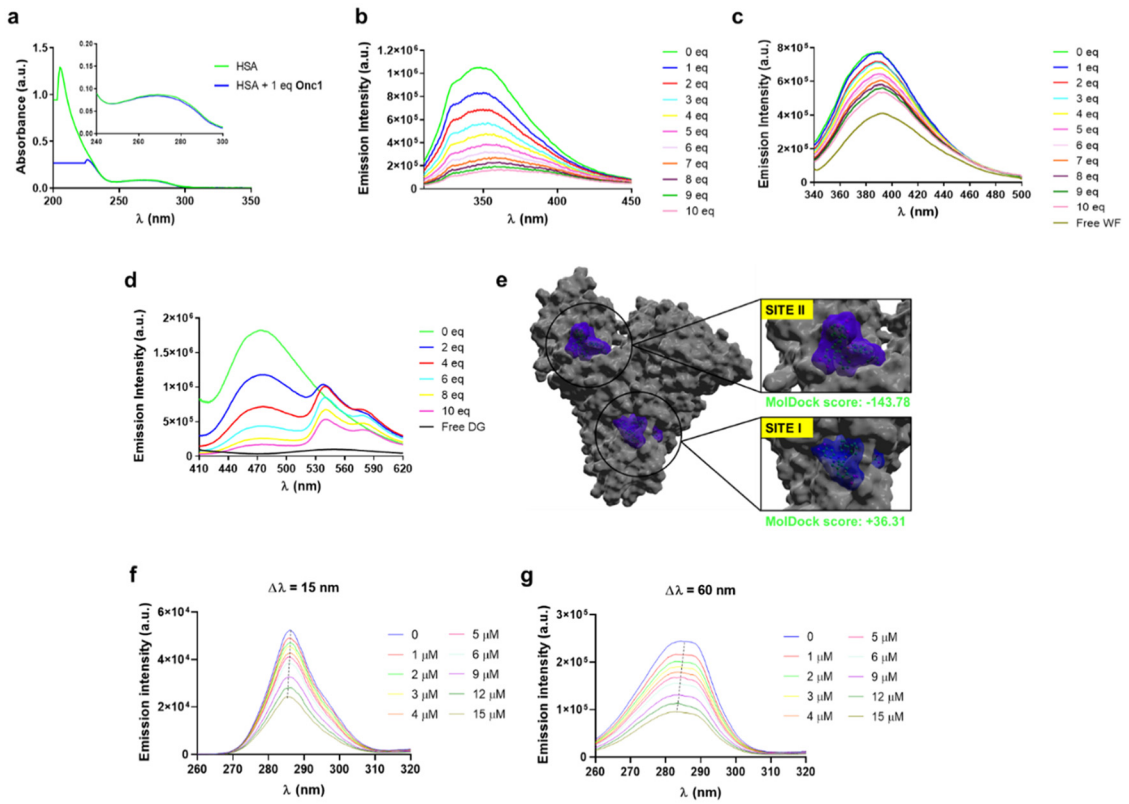

Fig. 5 (a) Absorption spectra of HSA upon incubation with one equivalent of **Onc1**. (b) Emission spectra of HSA upon successive addition of **Onc1**. (c) Emission spectra of the preformed warfarin–HSA adduct (site I binding) upon successive addition of **Onc1**. (d) Emission spectra of the preformed dansyl glycine–HSA adduct (site II binding) upon successive addition of **Onc1**. (e) Docking simulation of the binding of **Onc1** at HSA. (f) Monitoring of the synchronous fluorescence spectra of HSA (3 μM) at $\Delta\lambda$ = 15 nm upon cumulative additions of **Onc1** (0–15 μM). Recorded range: 260–320 nm. (g) Monitoring of the synchronous fluorescence spectra of HSA (3 μM) at $\Delta\lambda$ = 60 nm upon cumulative additions of **Onc1** (0–15 μM). Recorded range: 260–320 nm.

indicating the optimal positioning of the compound (Fig. 5e). However, when the docking was restricted to specific subpockets, **Onc1** exhibited binding at site I with a twisted coordination geometry and a positive docking score, suggesting an unfavorable interaction, and at site II a highly negative docking score, indicating favorable binding. Further analysis of the binding of **Onc1** in site II revealed the presence of attractive electrostatic forces, hydrogen bonding, and hydrophobic van der Waals interactions stabilizing the **Onc1**–HSA adduct (Fig. S36–S40; summary of docking parameters: Table S5). Overall, these results suggest the preferential binding of **Onc1** in site II of HSA.

To gain further insight about protein structural changes while bound to **Onc1**, synchronous emission experiments were performed. This spectrophotometric technique can give valuable information about conformational changes in the hydrophobic environments of proteins. As albumin's fluorescence predominantly arises from tryptophan (Trp) and tyrosine (Tyr) residues, the difference between excitation and emission wavelengths ($\Delta\lambda = \lambda_{em} - \lambda_{exc}$) can reflect their different emissive nature. If $\Delta\lambda$ = 15 nm, the synchronous spectrum depicts the emission arising from tyrosine residues, whereas a $\Delta\lambda$ = 60 nm difference is characteristic of the Trp214 residue.[55] The synchronous fluorescence spectra of HSA at $\Delta\lambda$ = 15 nm (Fig. 5f) and $\Delta\lambda$ = 60 nm (Fig. 5g) upon incubation with increasing amounts of complex **Onc1** underwent noticeable hypochromic and hypsochromic effects, thus suggesting the capability of this complex to alter both tryptophan- and tyrosine-contributing hydrophobic environments. Further theoretical analysis with molecular docking calculations matched with the experimental studies, as **Onc1** was found to allocate in the vicinity of tryptophan (Trp214) and several tyrosine residues (Tyr30, Tyr 84, Tyr 140, Tyr148, Tyr150, Tyr401, Tyr411, Tyr452 and Tyr497) within albumin's tertiary structure (Fig. S41).

Besides non-covalent hydrophobic, electrostatic and hydrogen bonding interactions, metallodrugs have previously shown their ability to covalently bind to albumin through accessible thiol-containing cysteine residues.[18,23,24,56] To investigate the potential covalent binding of **Onc1** to albumin, a competitive fluorimetric binding was conducted. Albumin was incubated with CellTracker^{AM} Red CMTPX dye, commonly employed in biological experiments for viable cell tracking. This probe, originally a weak emitter, profusely reacts with any accessible thiol groups of cysteine-bearing proteins, yielding a red fluorescent thioether adduct. After incubation of the dye with albumin for 4 h, the emission spectrum of the red-emitting adduct was monitored upon incrementing amounts of complex **Onc1**. As observed, no significant changes could be detected, evidencing the inability of the iridium(III) complex to displace the dye and thereby suggesting that covalent binding to albumin is unlikely to happen (Fig. 6).

To further support this trend, **Onc1** was incubated with model *N*-acetyl cysteine at 37 °C at different times. No evident traces of the adduct could be detected neither by ^{1}H-NMR spectroscopy (Fig. S42) nor high-resolution electron spray ionization mass spectrometry (Fig. S43), therefore dismissing

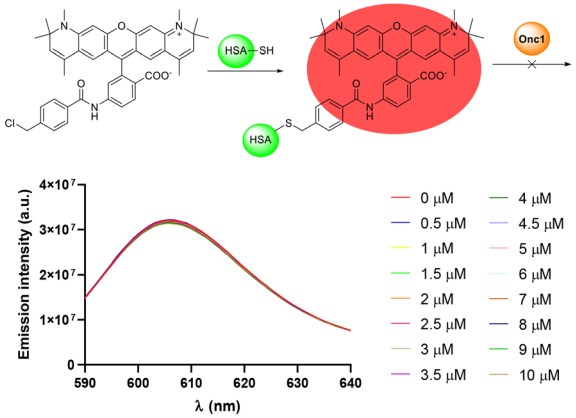

Fig. 6 Monitoring of the emission profile of the red-emitting adduct formed between HSA (5 μM) and CellTracker^{AM} CMTPX (5 μM) dye upon incubation with successive additions of **Onc1** (0–10 μM). Time between measurements: 5 min. λ_{exc} = 577 nm, registering range: 590–640 nm.

the formation of thiol-mediated covalent bonds with human serum albumin.

Preparation of the metal–albumin conjugate (Onc1@HSA)

Based on the strong interaction of **Onc1** with HSA, the respective nanoconjugate, followingly referred to as **Onc1@HSA**, was prepared on synthetic scale. **Onc1** was added dropwise to an aqueous solution of HSA and the reaction mixture exposed to dialysis to remove any traces of non-encapsulated metal complex. A direct comparison of aqueous solutions of **Onc1** and **Onc1@HSA** at the same concentration clearly demonstrated the superior water solubility of the **Onc1@HSA** conjugate (Fig. S44).

Absorption spectroscopy measurements revealed a conjugation efficiency of **Onc1** to HSA of approximately 80% (Fig. S45). Dynamic light scattering analysis of the **Onc1@HSA** nanoparticles indicated an average hydrodynamic diameter of 160 nm (Fig. S46a). The stability of the nanoparticles was evaluated by monitoring their size in aqueous solution over several days (Fig. S46b). No significant changes observed, suggesting high stability of **Onc1@HSA** in water.

The stability of the newly formed albumin conjugate nanoparticles was also studied by UV/VIS absorption spectroscopy by monitoring the metal-involved charge transfer absorption band (λ_{abs} = 435 nm). **Onc1@HSA** was found to be stable in the dark within neutral, acidic, basic, and reductive environments (approximately 80% of the iridium content was retained), whereas the fraction of conjugated iridium complex drastically decreased upon light irradiation (Fig. 7 and Fig. S47 and S48).

Further analysis of the albumin conjugate with ESI-MS suggested the non-covalent nature of the binding between **Onc1** and HSA, since the *m*/*z* peak of the resulting adduct could not be detected in the mass spectrum (Fig. S49). This finding may be attributable to the harsh ionization and electron impact process, possibly leading to the break of the

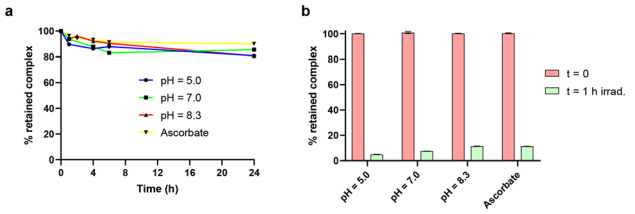

Fig. 7 Stability of **Onc1@HSA** (50 μM) in neutral (phosphate-buffered saline, 10 mM, pH = 7.0), acidic (acetate buffer, 100 mM, pH = 5.0), basic (HEPES buffer, 50 mM, pH = 8.3) and reductive (sodium ascorbate, 10 mM) aqueous solutions in the dark (a) or upon light irradiation for 1 h with a blue lamp (1 h, λ = 465 nm, 5 mW cm^{-2}) (b). Three independent measurements were carried out.

non-covalent conjugate. To support this evidence, the mass spectrum was recorded in the 200–3000 *m*/*z* range, observing free **Onc1** complex. As the samples were dialyzed prior to conduct the measurement, detection of free complex strongly suggests the breakage of **Onc1@HSA** during ionization and electron impact.

The octanol/phosphate-buffered saline partition coefficient (log *P*) was determined using the spectrophotometric 'shake-flask' method. The log *P* value for **Onc1@HSA** was found to be −0.56 ± 0.14, indicating it is significantly more hydrophilic than **Onc1** (log *P* = 1.42 ± 0.03) (Table S6). Photophysical evaluation of the albumin conjugate showed no distinguishable changes in the absorption and emission spectra of **Onc1@HSA** with those obtained for the parent complex **Onc1** (Fig. S50 and S51). Photochemical evaluation of **Onc1@HSA** showed the ability of the albumin conjugate to produce singlet oxygen upon light irradiation, as the emission intensity of the singlet oxygen sensor green (SOSG) probe underwent an increase with the continuous irradiation at short intervals (Fig. S52).

In vitro (photo)-cytotoxicity

Based on the promising photophysical and photochemical properties of the albumin conjugate **Onc1@HSA**, its biological (photo-)activity was evaluated in cancerous murine colon carcinoma (CT-26), human breast adenocarcinoma (MCF-7), human hepatocellular carcinoma (Hep G2), and non-cancerous human fibroblast (GM-5657) cells. The therapeutic effect was compared to the parent complex **Onc1**, the clinically-approved chemotherapeutic drug cisplatin, and the clinically-approved photosensitizer Photofrin (Table 1). The (photo-)toxicity of the tested compounds was evaluated by the 3-(4,5-dimethylthiazol-2-yl)-2,5-diphenyltetrazolium bromide (MTT) assay. The cells were treated with increasing concentrations of the compounds for 4 h, the media was refreshed, the cells were kept in the dark or exposed to irradiation (450 nm, power: 20%, 10 min, 1.2 J cm^{-2}), and after an additional 44 h the cell viability determined. The molecular metal complex **Onc1** was found to be non-toxic in the dark as well as upon irradiation (IC_{50} > 100 μM) in all investigated cell lines. Strikingly, while **Onc1@HSA** demonstrated to be non-toxic in the dark ($IC_{50,dark}$ > 100 μM), matching with the stability of the albumin conjugate, where the complex remains inactive whilst trapped by the protein. In contrast, the compound showed a strong therapeutic response upon irradiation ($IC_{50,light}$ = 1.17–2.93 μM) in cancerous cells, achieving a high phototoxic index (PI > 86). Importantly, **Onc1@HSA** showed to be less cytotoxic to the non-cancerous GM-5657 cells. The phototoxic index of **Onc1@HSA** was found to be higher than for the clinically applied photosensitizer Photofrin for all cell lines under identical conditions.

Cellular uptake pathway

The cellular uptake of the **Onc1** complex and its corresponding albumin conjugate, **Onc1@HSA**, was subsequently analyzed using fluorescence microscopy. Microscopy images revealed a significantly enhanced accumulation of **Onc1@HSA** compared to **Onc1**. These observations provide a rationale for the absence of a cytotoxic response from **Onc1** and suggest that conjugation with HSA effectively enhances the internalization of the iridium(III) complex into cells (Fig. S53). Using inductively coupled plasma optical emission spectroscopy, the uptake of **Onc1@HSA** inside the cell was quantified to be 38 ± 4 ng per million of cells. Followingly, the uptake mechanism of the compounds was investigated by selectively inhibiting various cellular transport pathways using metabolic inhibitors (2-deoxy-D-glucose and oligomycin), endocytosis inhibitors (ammonium chloride or chloroquine), cationic transporter inhibitor (tetraethylammonium chloride), and as well as incubation at reduced temperature (4 °C), and then monitoring of the internalization of the nanoparticles by fluorescence microscopy. While metabolic and endocytosis inhibitors had no significant effect on the uptake, these pathways were ruled out as major contributors. In contrast, preincubation with the

Table 1 IC_{50} values (μM) of **Onc1**, **Onc1@HSA**, cisplatin and photofrin in cancerous murine colon carcinoma (CT-26), human breast adenocarcinoma (MCF-7), human hepatocellular carcinoma (Hep G2), and non-cancerous human fibroblast (GM-5657) cells. Light exposure: 450 nm, power: 20%, 10 min, 1.2 J cm^{-2}. Data is expressed as the average of three independent measurements (mean ± standard deviation)

	CT-26			MCF-7			Hep G2			GM-5657		
	Dark	Light	PI	Dark	Light	PI	Dark	Light	PI	Dark	Light	PI
Onc1	>100	>100	—	>100	>100	—	>100	>100	—	>100	>100	—
Onc1@HSA	>100	1.17 ± 0.07	>86	>100	1.56 ± 0.09	>64	>100	2.9 ± 0.15	> 34	>100	18.43 ± 1.71	>5
Cisplatin	6.16 ± 0.71	—	—	6.38 ± 0.92	—	—	7.35 ± 0.84	—	—	9.74 ± 1.13	—	—
Photofrin	>20	3.70 ± 0.43	>5	>20	2.77 ± 0.68	>7	>20	6.19 ± 0.85	>3	>20	4.48 ± 0.56	>4

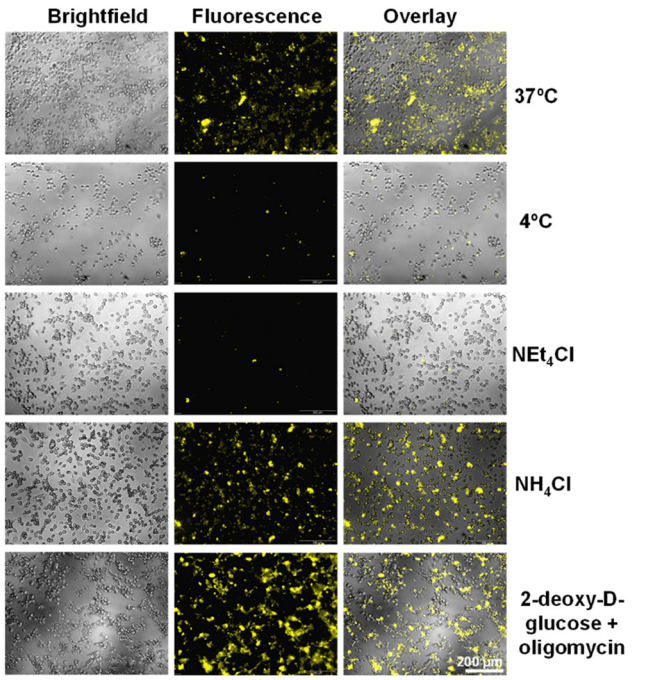

Fig. 8 Fluorescence microscopy images of CT-26 cells upon pre-incubation at 37 °C (control), 4 °C (inhibition of the active transport), with 2-deoxy-D-glucose and oligomycin (metabolic inhibitors), ammonium chloride (endocytosis inhibitor), tetraethylammonium chloride (cation transporter inhibitor), and followingly incubated with **Onc1@HSA**. λ_{ex} = 460–490 nm, λ_{em} = 590 nm, scale bar = 200 µm.

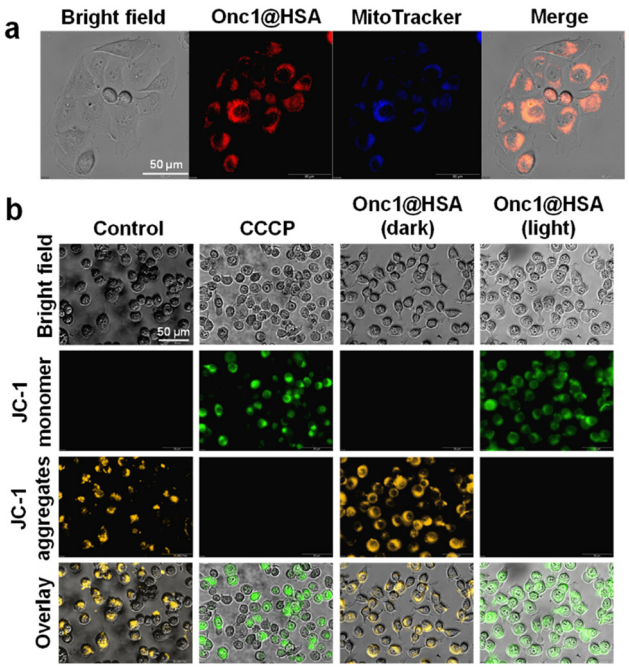

Fig. 9 (a) Confocal laser scanning microscopy images of CT-26 cells upon co-incubation of **Onc1@HSA** (λ_{ex} = 405 nm, λ_{em} = 635 nm) and BioTracker 405 Blue Mitochondrial Dye (λ_{ex} = 405 nm, λ_{em} = 440 nm). Scale bar = 50 µm. (b) Fluorescence microscopy images of CT-26 cells upon co-incubation of **Onc1@HSA** and the JC-1 probe (JC-1 monomers: λ_{ex} = 460–490 nm, λ_{em} = 510–550 nm; JC-1 aggregates: λ_{ex} = 460–490 nm, λ_{em} = 590 nm). Scale bar = 50 µm. Carbonyl cyanide chlorophenyl hydrazone (CCCP) was used as a positive control.

cationic transporter inhibitor and incubation at reduced temperature resulted in a markedly decreased uptake of **Onc1@HSA** (Fig. 8). These findings align with literature reports indicating that the internalization of the drug–albumin conjugate can be actively mediated by overexpressed receptor proteins, such as the secreted protein acidic and rich in cysteine (SPARC) protein, which possesses a binding site for cations and it has showed to facilitate the accumulation of other metallodrug–albumin conjugates.[57–60]

Cellular localization and mitochondrial membrane depolarization

The subcellular localization of **Onc1@HSA** was examined using confocal laser scanning microscopy. The emission pattern of the compound was compared with that of commercial dyes targeting major cellular organelles. Microscopy images revealed a high degree of colocalization between the emission pattern of **Onc1@HSA** and that of BioTracker 405 Blue Mitochondrial Dye (Fig. 9a), indicating preferential accumulation in the mitochondria. As a complementary approach, the subcellular distribution of **Onc1@HSA** was quantitatively assessed by measuring the iridium content in isolated organelles using inductively coupled plasma optical emission spectroscopy. The analysis revealed that only a small fraction of the internalized compound localized to the nucleus (5 ± 3%), while the majority accumulated in the mitochondria (58 ± 7%), corroborating the results obtained from confocal laser scanning microscopy. Subsequently, the ability of **Onc1@HSA** to induce mitochondrial membrane depolarization was assessed using the specific fluorescent probe JC-1. While no changes in mitochondrial membrane potential were observed following treatment with the conjugate in the dark, significant depolarization was detected upon treatment and irradiation with light (Fig. 9b).

Cellular ROS generation and NADH Oxidation

The ability of **Onc1@HSA** to generate ROS was investigated by fluorescence microscopy using the specific probe 2′,7′-dichlorodihydrofluorescein diacetate. Whereas no emission was observed when cells were treated with **Onc1@HSA** in the dark, green emission was detected when cells were exposed to light irradiation, suggesting the photo-catalytic production of ROS by **Onc1@HSA** (Fig. 10). The photocatalytic oxidation of NADH inside the cancer cells was studied using a commercial NADH/NAD+ assay kit upon treatment in the dark and upon irradiation. While no changes upon treatment in the dark were observed, upon treatment with **Onc1@HSA** and light irradiation the normalized NADH/NAD^+ ratio in the untreated cells dropped to 0.61 ± 0.04, indicative of the conversion of cellular NADH levels.

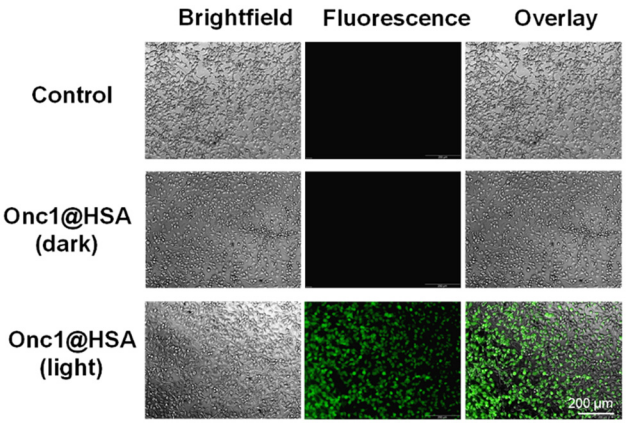

Fig. 10 Evaluation of the formation of reactive oxygen species (ROS) in CT-26 cells by fluorescence microscopy upon treatment with **Onc1@HSA** (10 μM) and exposure to blue (450 nm, power: 20%, 10 min, 1.2 J cm^{-2}) light irradiation.

Cell death mechanism

The mechanism of cell death induced by the conjugate **Onc1@HSA** was investigated using flow cytometry. Cancer cells were treated with **Onc1@HSA** either in the dark or under light exposure, followed by staining with Annexin V-FITC and 7-aminoactinomycin to assess apoptotic and necrotic responses. While no significant effects were observed in the dark, light exposure triggered a therapeutic response characterized by the externalization of phosphatidylserine to the outer leaflet of the plasma membrane and disruption of the cell membrane. Notably, pretreatment with a necroptosis inhibitor did not restore cell viability, ruling out necroptosis as the underlying mechanism of cell death (Fig. 11a). Furthermore, fluorescence microscopy confirmed cell membrane disruption upon **Onc1@HSA** treatment and light irradiation (Fig. 11b). To assess the potential involvement of caspase-1 in the cell death mechanism, cancer cells were preincubated with the caspase-1

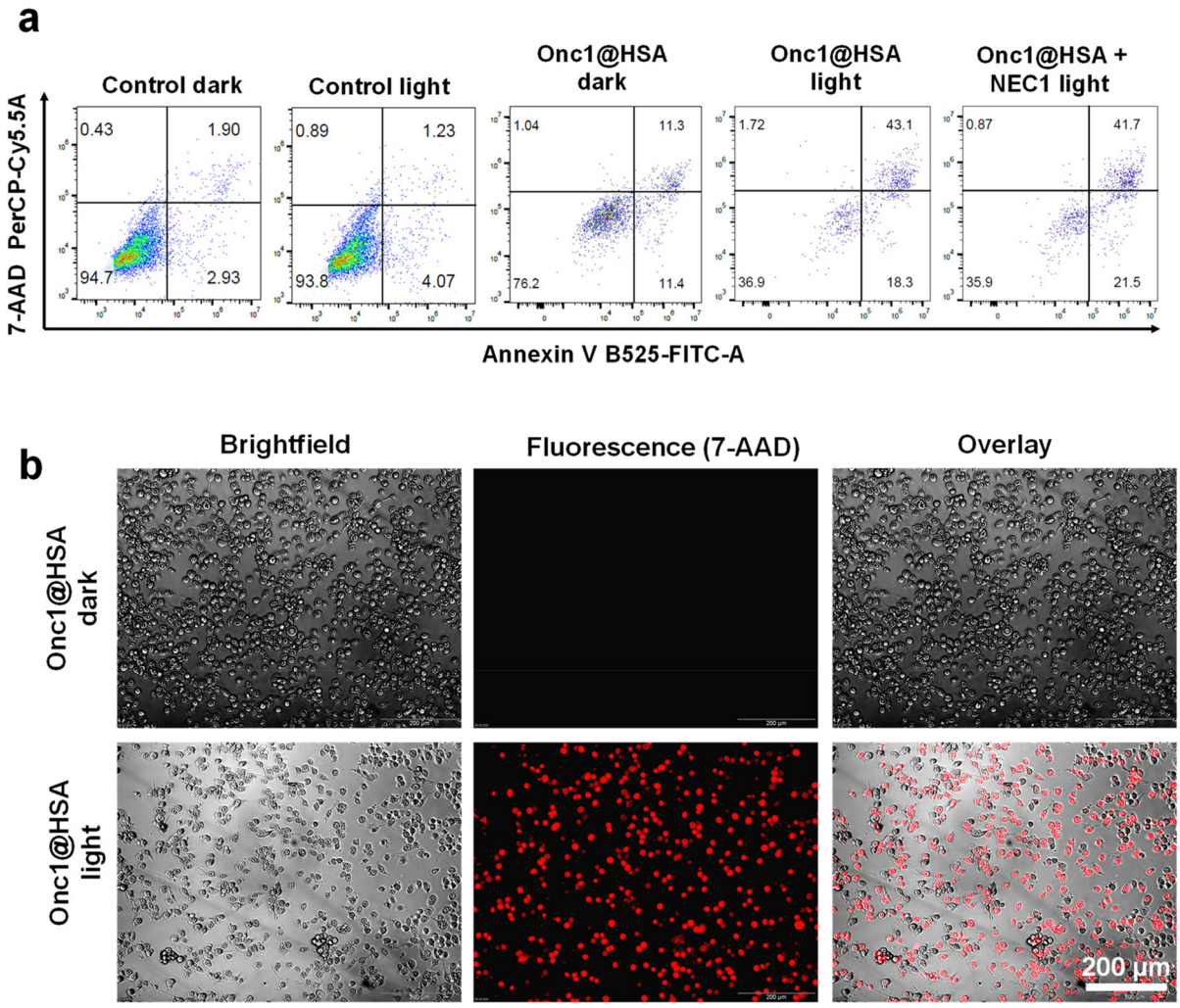

Fig. 11 (a) Flow cytometry analysis of CT-26 cells upon incubation with Annexin V-FITC/7-aminoactinomycin and treatment with **Onc1@HSA** in the dark or exposure to irradiation (450 nm, power: 20%, 10 min, 1.2 J cm^{-2}). (b) Fluorescence microscopy images of CT-26 cells upon incubation with 7-aminoactinomycin and treatment with **Onc1@HSA** in the dark or exposure to irradiation (450 nm, power: 20%, 10 min, 1.2 J cm^{-2}). Scale bar = 200 μm.

inhibitor Belnacasan, followed by treatment with the IC_{50} concentration of **Onc1@HSA**. No significant change in cell viability was observed under dark (non-activated) conditions. However, upon activation, a modest increase in cell survival to 67 ± 5% was observed with Belnacasan preincubation, suggesting that caspase-1 may contribute partially to the observed cytotoxicity.

Cell morphology

To gain further insight, the morphological changes of the cancer cells upon treatment with **Onc1@HSA** were analyzed using light microscopy. Upon light exposure, cells exhibited characteristic swelling and rounding (green arrows), followed by cytoplasmic vacuolization and the formation of organelle-free blisters (yellow arrow). These blisters appeared empty, distinguishing them from those observed in apoptotic cells. Additionally, bright-field imaging revealed chromatin clumping (red arrows), evidenced by the presence of dense black spots in the nuclear region (Fig. 12). In contrast, no significant morphological alterations were observed in untreated cells (Fig. S54).

Intracellular ATP and Ca^{2+} levels

Changes in ATP levels following treatment were assessed using the CellTiter-Glo luminescent assay. While treatment in the dark had no significant effect, exposure to **Onc1@HSA** combined with irradiation led to a substantial depletion of ATP (Fig. 13a). Additionally, intracellular Ca^{2+} levels were monitored by fluorescence microscopy using the Ca^{2+}-specific probe Fluo-4 AM. Microscopy images revealed an increase in green fluorescence intensity upon treatment with **Onc1@HSA**, indicating elevated intracellular Ca^{2+} levels (Fig. 13b). The depletion of ATP and the release of Ca^{2+} typically induces the activation of calpain proteins that cleave key cytoskeletal and membrane-associated proteins. To investigate these effects, the cancer cells were preincubated with calpain inhibitor Calpeptin, treated with the IC_{50} value of **Onc1@HSA**, and the cell viability determined. While no effect upon treatment in the dark was observed, an enhancement in the cell survival upon preincubation with the calpain inhibitor to 71 ± 4% was observed, indicative that the cell death mechanism is related to calpain activation. Taken together, the observed cellular swelling, cytoplasmic vacuolization, formation of organelle-free blisters, ATP depletion, and Ca^{2+} release strongly suggest that **Onc1@HSA** induces an oncosis cell death mechanism upon light activation.

3D multicellular tumor spheroids

Based upon the promising results obtained from two-dimensional monolayer cancer cell studies, the therapeutic effects of **Onc1@HSA** were further evaluated in three-dimensional multicellular tumor spheroids. Tumor spheroids are able to simulate the pathological conditions of solid tumors like hypoxic centers, proliferations gradients, or nutrients gradients.[61] To assess the (photo-)therapeutic efficacy, a fluorometric assay utilizing the CellTiter-Glo® 3D Cell Viability kit was conducted. The results revealed that **Onc1@HSA** exhibited low cytotoxicity in the dark (IC_{50} = 27.13 ± 1.20 μM); however, upon irradiation, a potent therapeutic response was observed in the low micromolar range (IC_{50} = 3.20 ± 0.92 μM) (overview:

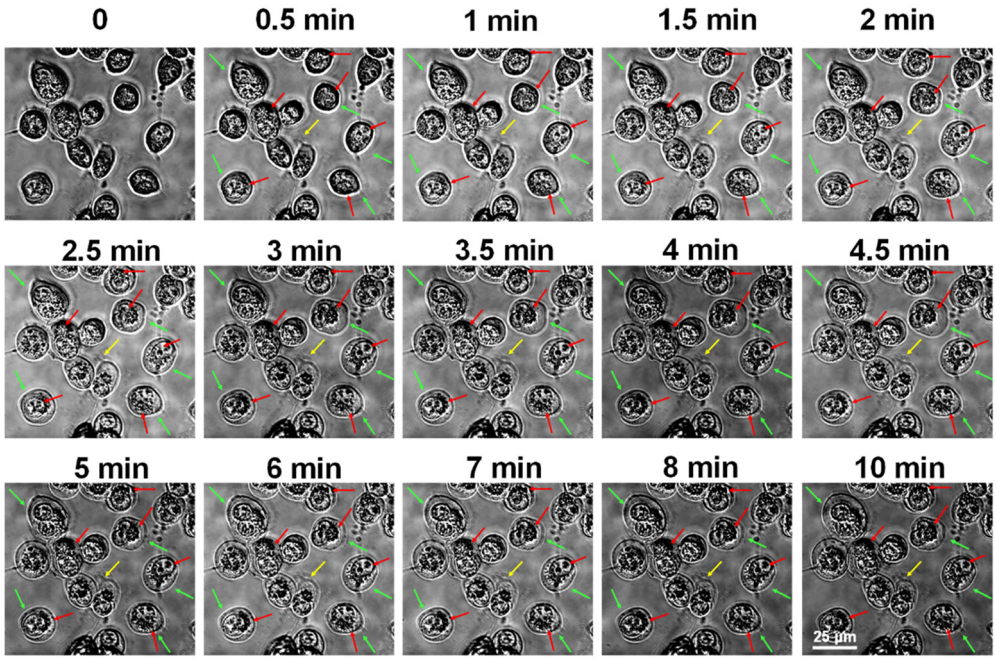

Fig. 12 Time-dependent light microscopy images of CT-26 cells upon treatment with **Onc1@HSA** and exposure to irradiation (λ_{irrad} = 460–490 nm). Scale bar = 25 μm.

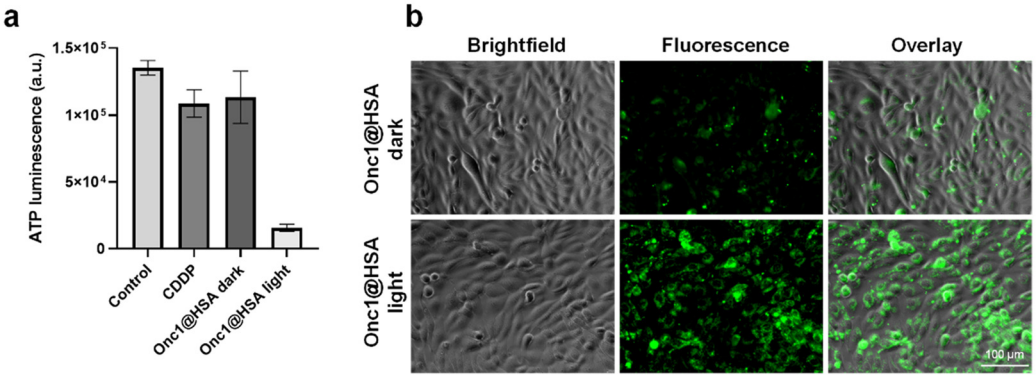

Fig. 13 (a) Measurement of the ATP luminescence of CT-26 cancer cells upon incubation at 37 °C (untreated cells, control) and treatment with cisplatin (CDDP) or **Onc1@HSA** in the dark or upon blue light (450 nm, power: 20%, 10 min, 1.2 J cm^{-2}) irradiation. (b) Ca^{2+} intracellular levels in **Onc1@HSA**-treated CT-26 cells qualitatively detected by fluorescence microscopy using the Fluo-4 AM probe. Scale bar: 100 μm.

Table S7, drug dose–response curves: Fig. S55). To visualize the (photo-)toxic activity of **Onc1@HSA**, light microscopy images of tumor spheroids with an average diameter of 300 μm were recorded two days after treatment with cisplatin, photofrin, or **Onc1@HSA** in the dark or upon light irradiation. While the treatment with cisplatin was found not to affect the size and morphology of the tumor spheroids, due to the use of low compound concentrations, a reduction in tumor size was observed upon treatment with **Onc1@HSA** and Photofrin exposure to irradiation (Fig. 14).

For a better understanding of the (photo-)toxicity mechanism against MCTS, the ability of **Onc1@HSA** to produce ROS species was evaluated by fluorescence microscopy using the specific probe 2′,7′-dichlorodihydrofluorescein diacetate (H_2DCFDA) (Fig. S56). The fluorescence images show a significant enhancement in the probe emission intensity when spheroids were treated with **Onc1@HSA** and subjected to light irradiation, indicating an efficient ROS generation. Notably, these ROS species were detected in the center of the spheroids, corroborating the results obtained for the growth inhibition assay.

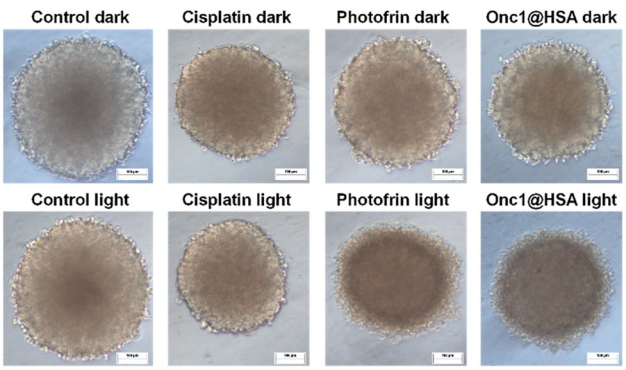

Fig. 14 Light microscopy images of CT-26 multicellular tumor spheroids after treatment with cisplatin, photofrin, or **Onc1@HSA** in the dark or upon irradiation (450 nm, power: 20%, 10 min, 1.2 J cm^{-2}). Scale bar = 100 μm.

Conclusions

In summary, this study reports on the chemical synthesis and biological evaluation of a cyclometalated Ir(III) complex conjugated to human serum albumin as a photosensitizer for oncosis-mediated photodynamic therapy. The conjugate exhibited negligible toxicity in the dark but demonstrated potent photocatalytic activity upon light irradiation, effectively oxidizing NADH and generating singlet oxygen. This resulted in a strong cytotoxic response against a variety of cancer cells and multicellular tumor spheroids, with a phototoxicity value in the very low micromolar range. Further mechanistic investigations revealed that the conjugate preferentially accumulated in mitochondria, where it induced NADH oxidation, triggered oxidative damage to the cell membrane, depleted intracellular ATP, and stimulated Ca^{2+} influx. These events led to characteristic morphological changes, including cellular swelling, cytoplasmic vacuolization, and the formation of organelle-free blisters, ultimately culminating in cell death by oncosis. Additionally, the albumin conjugate was found to exert a significant phototoxic activity in multicellular tumor spheroids. To the best of our knowledge, this study reports on the first example of a metal complex conjugated to human serum albumin as a photosensitizer for oncosis-mediated photodynamic therapy. We believe that the conjugation to human serum albumin could provide a strategy for the tumor selective treatment of cancerous tumors. We are confident that these findings could open new avenues towards the treatment of (apoptosis-) resistant tumors.

Author contributions

J. Karges, J. Ruiz and V. Rodríguez designed the project. A. Linero-Artiaga conducted the synthesis and the characterization of both the complex and the albumin conjugate. L.-M. Servos performed the DFT calculations. A. Linero-Artiaga carried out the biological experiments with the assistance of Z. Papadopoulos. A. Linero-Artiaga, J. Karges, J. Ruiz

and V. Rodríguez wrote the manuscript with all the analyzed data. All authors further discussed the results and revised the manuscript.

Conflicts of interest

The authors declare no competing interests.

Data availability

The data supporting this article have been included as part of the SI. Materials and instrumentation, synthetic methods for the preparation of proligand **1**, iridium species **2** and **Onc1**, and the theoretical and biological protocols have been added. Supporting figures and tables include a figure with reported metal-based oncosis inducers, a synthetic scheme, nuclear magnetic resonance (NMR) spectra, with the assignation of proton and carbon signals, mass spectrometry and HPLC analysis of complex **Onc1**, a detailed photophysical characterization, assisted by DFT calculations, the photochemical evaluation, interaction studies with human serum albumin (HSA), assisted by molecular docking calculations, the preparation and characterization of **Onc1@HSA** nanoparticles, and the photo-(cytotoxic) experiments conducted. See DOI: **https://doi.org/10.1039/d5qi01287b**

Acknowledgements

J. Karges gratefully acknowledges the financial support provided by the Liebig fellowship from the Chemical Industry Fund of the German Chemical Industry Association, the Life Sciences Bridge Award from the Aventis Foundation, Dr Otto Röhm Gedächtnisstiftung Award from the Dr. Otto Röhm Gedächtnisstiftung Foundation, and the Paul Ehrlich & Ludwig Darmstaedter Early Career Award 2024 – a prize awarded by the Paul Ehrlich Foundation, Germany. The authors thank Dr Carlos Plaza Sirvent (Ruhr University Bochum, Germany) for his assistance with flow cytometry analyses. The research of A. Linero-Artiaga, V. Rodríguez and J. Ruiz was supported by the Spanish Ministerio de Ciencia e Innovación-Agencia Estatal de Investigación (MCI/AEI/10.13039/501100011033) and FEDER funds (project PID2021-122850NB-I00). A. L.-A. thanks the University of Murcia for his predoctoral grant (100159/2021). This article is based upon work from COST Action CA22131, LUCES Supramolecular LUminescent Chemosensors for Environmental Security, supported by COST (European Cooperation in Science and Technology).

References

1 S. Monro, K. L. Colón, H. Yin, J. I. Roque, P. Konda, S. Gujar, R. P. Thummel, L. Lilge, C. G. Cameron and S. A. McFarland, Transition Metal Complexes and Photodynamic Therapy from a Tumor-Centered Approach: Challenges, Opportunities and Highlights from the Development of TLD1433, *Chem. Rev.*, 2019, **119**, 797.
2 C. Imberti, P. Zhang, H. Huang and P. J. Sadler, New Designs for Phototherapeutic Transition Metal Complexes, *Angew. Chem., Int. Ed.*, 2020, **59**, 61.
3 J. Karges, Clinical Development of Metal Complexes as Photosensitizers for Photodynamic Therapy of Cancer, *Angew. Chem., Int. Ed.*, 2022, **61**, e202112236.
4 H. Shi, R. C. Marchi and P. J. Sadler, Advances in the Design of Photoactivatable Metallodrugs: Excited State Metallomics, *Angew. Chem., Int. Ed.*, 2025, **64**, e202423335.
5 N. Kwon, H. Weng, M. A. Rajora and G. Zheng, Activatable Photosensitizers: From Fundamental Principles to Advanced Designs, *Angew. Chem., Int. Ed.*, 2025, **64**, e202423348.
6 Y. You and W. Nam, Photofunctional triplet excited states of cyclometalated Ir(III) complexes: beyond electroluminescence, *Chem. Soc. Rev.*, 2012, **41**, 7061.
7 H. Huang, S. Banerjee, K. Qiu, P. Zhang, O. Blacque, T. Malcomson, M. J. Paterson, G. J. Clarkson, M. Staniforth, V. G. Stavros, G. Gasser, H. Chao and P. J. Sadler, Targeted photoredox catalysis in cancer cells, *Nat. Chem.*, 2019, **11**, 1041.
8 V. Novohradsky, A. Rovira, C. Hally, A. Galindo, G. Vigueras, A. Gandioso, M. Svitelova, R. Bresolí-Obach, H. Kostrhunova, L. Markova, J. Kasparkova, S. Nonell, J. Ruiz, V. Brabec and V. Marchán, Towards Novel Photodynamic Anticancer Agents Generating Superoxide Anion Radicals: A Cyclometalated IrIII Complex Conjugated to a Far-Red Emitting Coumarin, *Angew. Chem., Int. Ed.*, 2019, **58**, 6311.
9 L. C.-C. Lee and K. K.-W. Lo, Luminescent and Photofunctional Transition Metal Complexes: From Molecular Design to Diagnostic and Therapeutic Applications, *J. Am. Chem. Soc.*, 2022, **144**, 14420.
10 L. C.-C. Lee and K. K.-W. Lo, Leveraging the Photofunctions of Transition Metal Complexes for the Design of Innovative Phototherapeutics, *Small Methods*, 2024, **8**, 2400563.
11 T. Kench, A. Rahardjo, G. G. Terrones, A. Bellamkonda, T. E. Maher, M. Storch, H. J. Kulik and R. Vilar, A Semi-Automated, High-Throughput Approach for the Synthesis and Identification of Highly Photo-Cytotoxic Iridium Complexes, *Angew. Chem., Int. Ed.*, 2024, **63**, e202401808.
12 L. C.-C. Lee and K. K.-W. Lo, Shining New Light on Biological Systems: Luminescent Transition Metal Complexes for Bioimaging and Biosensing Applications, *Chem. Rev.*, 2024, **124**, 8825.
13 L. Ke, F. Wei, L. Xie, J. Karges, Y. Chen, L. Ji and H. Chao, A Biodegradable Iridium(III) Coordination Polymer for Enhanced Two-Photon Photodynamic Therapy Using an Apoptosis–Ferroptosis Hybrid Pathway, *Angew. Chem., Int. Ed.*, 2022, **61**, e202205429.
14 M. Redrado, Z. Xiao, K. Upitak, B.-T. Doan, C. M. Thomas and G. Gasser, Applications of Biodegradable Polymers in the Encapsulation of Anticancer Metal Complexes, *Adv. Funct. Mater.*, 2024, **34**, 2401950.

15 G. Liang, N. Montesdeoca, D. Tang, B. Wang, H. Xiao, J. Karges and K. Shang, Facile one-pot synthesis of Ir(III) Bodipy polymeric gemini nanoparticles for tumor selective NIR photoactivated anticancer therapy, *Biomaterials*, 2024, **309**, 122618.

16 B. Das, Transition Metal Complex-Loaded Nanosystems: Advances in Stimuli-Responsive Cancer Therapies, *Small*, 2025, **21**, 2410338.

17 S. Chakrabortty, B. K. Agrawalla, A. Stumper, N. M. Vegi, S. Fischer, C. Reichardt, M. Kögler, B. Dietzek, M. Feuring-Buske, C. Buske, S. Rau and T. Weil, Mitochondria Targeted Protein-Ruthenium Photosensitizer for Efficient Photodynamic Applications, *J. Am. Chem. Soc.*, 2017, **139**, 2512.

18 P. Zhang, H. Huang, S. Banerjee, G. J. Clarkson, C. Ge, C. Imberti and P. J. Sadler, Nucleus-Targeted Organoiridium–Albumin Conjugate for Photodynamic Cancer Therapy, *Angew. Chem., Int. Ed.*, 2019, **58**, 2350.

19 H. Schueffl, S. Theiner, G. Hermann, J. Mayr, P. Fronik, D. Groza, S. van Schonhooven, L. Galvez, N. S. Sommerfeld, A. Schintlmeister, S. Reipert, M. Wagner, R. M. Mader, G. Koellensperger, B. K. Keppler, W. Berger, C. R. Kowol, A. Legin and P. Heffeter, Albumin-targeting of an oxaliplatin-releasing platinum(IV) prodrug results in pronounced anticancer activity due to endocytotic drug uptake in vivo, *Chem. Sci.*, 2021, **12**, 12587.

20 P. Fronik, I. Poetsch, A. Kastner, T. Mendrina, S. Hager, K. Hohenwallner, H. Schueffl, D. Herndler-Brandstetter, G. Koellensperger, E. Rampler, J. Kopecka, C. Riganti, W. Berger, B. K. Keppler, P. Heffeter and C. R. Kowol, Structure–Activity Relationships of Triple-Action Platinum (IV) Prodrugs with Albumin-Binding Properties and Immunomodulating Ligands, *J. Med. Chem.*, 2021, **64**, 12132.

21 K. Imai, K. Muguruma, A. Nakamura, Y. Kusakari, T.-C. Chang, A. R. Pradipta and K. Tanaka, In Vivo Synthetic Anticancer Approach by Resourcing Mouse Blood Albumin as a Biocompatible Artificial Metalloenzyme, *Angew. Chem., Int. Ed.*, 2024, **63**, e202411225.

22 A. Linero-Artiaga, L.-M. Servos, V. Rodríguez, J. Ruiz and J. Karges, Rationally Designed Ir(III) Complex with an Exceptionally Strong Binding to Human Serum Albumin for Targeted Photodynamic Therapy, *J. Med. Chem.*, 2025, **68**, 7792.

23 M. Dijkstra, M. Gutmann, M. Gradl, A. Federa, C. Jaunecker, J. V. Breitenstein, P. Vician, C. Pirker, D. Valcanover, P. Heffeter, B. K. Keppler, W. Berger and C. R. Kowol, Albumin-targeted oxaliplatin(iv) prodrugs bearing STING agonists, *Inorg. Chem. Front.*, 2025, **12**, 4284.

24 M. Dijkstra, H. Schueffl, B. Adamova, O. Baumfried, A. Kastner, W. Berger, B. K. Keppler, P. Heffeter and C. R. Kowol, Exploring the Structure–Activity Relationships of Albumin-Targeted Picoplatin-Based Platinum(IV) Prodrugs, *Inorg. Chem.*, 2025, **64**, 2554.

25 L. Wenskowsky, H. Schreuder, V. Derdau, H. Matter, J. Volkmar, M. Nazaré, T. Opatz and S. Petry, Identification and Characterization of a Single High-Affinity Fatty Acid Binding Site in Human Serum Albumin, *Angew. Chem., Int. Ed.*, 2018, **57**, 1044.

26 X. Wang, L. Tian, Y. Li, W. Yao, J. Zhu, H. Zhou, G. Chen, T. Chen, Z. Liu, W. Tan and Y. Yang, Universal Albumin Drugs-Cored Spherical Nucleic Acid (ad-SNA) Platform for Targeted Drug Delivery, *Angew. Chem., Int. Ed.*, 2025, **64**, e202421949.

27 R. K. Pandey, S. Constantine, T. Tsuchida, G. Zheng, C. J. Medforth, M. Aoudia, A. N. Kozyrev, M. A. J. Rodgers, H. Kato, K. M. Smith and T. J. Dougherty, Synthesis, Photophysical Properties, in Vivo Photosensitizing Efficacy, and Human Serum Albumin Binding Properties of Some Novel Bacteriochlorins, *J. Med. Chem.*, 1997, **40**, 2770.

28 V. Margulis, R. P. Kaufman, G. Marcq, N. D. Shore, M. Colombel, E. M. Uchio, S. P. Psutka, M. Aller, S. Rausch, C. Raventos, A. Shvero, A. Mroz, N. Kudinova, Y. Cohen, I. Krasnopolskaya, G. Alpert, A. J. Scherz and J. Coleman, ENLIGHTED phase 3 study: Efficacy and safety of padeliporfin vascular targeted photodynamic therapy (VTP) for treatment of low-grade upper tract urothelial cancer (LG UTUC), *J. Clin. Oncol.*, 2024, **42**, TPS4622.

29 Y. Zhang, B.-T. Doan and G. Gasser, Metal-Based Photosensitizers as Inducers of Regulated Cell Death Mechanisms, *Chem. Rev.*, 2023, **123**, 10135.

30 H. Yuan, Z. Han, Y. Chen, F. Qi, H. Fang, Z. Guo, S. Zhang and W. He, Ferroptosis Photoinduced by New Cyclometalated Iridium(III) Complexes and Its Synergism with Apoptosis in Tumor Cell Inhibition, *Angew. Chem., Int. Ed.*, 2021, **60**, 8174.

31 T. Feng, Z. Tang, J. Karges, J. Shen, C. Jin, Y. Chen, Y. Pan, Y. He, L. Ji and H. Chao, Exosome camouflaged coordination-assembled Iridium(III) photosensitizers for apoptosis-autophagy-ferroptosis induced combination therapy against melanoma, *Biomaterials*, 2023, **301**, 122212.

32 Y.-L. Zeng, L.-Y. Liu, T.-Z. Ma, Y. Liu, B. Liu, W. Liu, Q.-H. Shen, C. Wu and Z.-W. Mao, Iridium(III) Photosensitizers Induce Simultaneous Pyroptosis and Ferroptosis for Multi-Network Synergistic Tumor Immunotherapy, *Angew. Chem., Int. Ed.*, 2024, **63**, e202410803.

33 X. Liu, T. Van Vleet and R. G. Schnellmann, The Role of Calpain in Oncotic Cell Death, *Annu. Rev. Pharmacol. Toxicol.*, 2004, **44**, 349.

34 P. Weerasinghe and L. M. Buja, Oncosis: An important non-apoptotic mode of cell death, *Exp. Mol. Pathol.*, 2012, **93**, 302.

35 D. Tang, R. Kang, T. V. Berghe, P. Vandenabeele and G. Kroemer, The molecular machinery of regulated cell death, *Cell Res.*, 2019, **29**, 347–364.

36 W. Park, S. Wei, B.-S. Kim, B. Kim, S.-J. Bae, Y. C. Chae, D. Ryu and K.-T. Ha, Diversity and complexity of cell death: a historical review, *Exp. Mol. Med.*, 2023, **55**, 1573–1594.

37 J. Guo, W. Yang, F. Mai, J. Liang, J. Luo, M. Zhou, D. Yu, Y. Wang and C. Li, Unravelling oncosis: morphological and molecular insights into a unique cell death pathway, *Front. Immunol.*, 2024, **15**, 2024.

38 R. Guan, Y. Chen, L. Zeng, T. W. Rees, C. Jin, J. Huang, Z.-S. Chen, L. Ji and H. Chao, Oncosis-inducing cyclometalated iridium(III) complexes, *Chem. Sci.*, 2018, **9**, 5183.

39 P. J. Jarman, F. Noakes, S. Fairbanks, K. Smitten, I. K. Griffiths, H. K. Saeed, J. A. Thomas and C. Smythe, Exploring the Cytotoxicity, Uptake, Cellular Response, and Proteomics of Mono- and Dinuclear DNA Light-Switch Complexes, *J. Am. Chem. Soc.*, 2019, **141**, 2925.

40 W. Wang, P. Wang, F. Shen, C. Gao and J. Yang, Turn-on Near-Infrared Phosphorescent Recognition of Anion Based on Self-Assembly of Cyclometalated Platinum Complexes That Induce Oncosis and Monitor Living Cells, *ACS Nano*, 2024, **18**, 5656.

41 J. Kasparkova, A. Hernández-García, H. Kostrhunova, M. Goicuría, V. Novohradsky, D. Bautista, L. Markova, M. D. Santana, V. Brabec and J. Ruiz, Novel 2-(5-Arylthiophen-2-yl)-benzoazole Cyclometalated Iridium(III) dppz Complexes Exhibit Selective Phototoxicity in Cancer Cells by Lysosomal Damage and Oncosis, *J. Med. Chem.*, 2024, **67**, 691.

42 T. Feng, Z. Tang, J. Shu, X. Wu, H. Jiang, Z. Chen, Y. Chen, L. Ji and H. Chao, A Cyclometalated Ruthenium(II) Complex Induces Oncosis for Synergistic Activation of Innate and Adaptive Immunity, *Angew. Chem., Int. Ed.*, 2024, **63**, e202405679.

43 C. D. Ertl, C. Momblona, A. Pertegás, J. M. Junquera-Hernández, M.-G. La-Placa, A. Prescimone, E. Ortí, C. E. Housecroft, E. C. Constable and H. J. Bolink, Highly Stable Red-Light-Emitting Electrochemical Cells, *J. Am. Chem. Soc.*, 2017, **139**, 3237.

44 S. DiLuzio, V. Mdluli, T. U. Connell, J. Lewis, V. VanBenschoten and S. Bernhard, High-Throughput Screening and Automated Data-Driven Analysis of the Triplet Photophysical Properties of Structurally Diverse, Heteroleptic Iridium(III) Complexes, *J. Am. Chem. Soc.*, 2021, **143**, 1179.

45 J.-H. Zhu, X. He, Y. Wu, H. Huang, D. Yang, J. Li, M. Gu, L. Wang, M. Li, X. Chen and X. Peng, Cyclometalated Iridium(III) Schiff Base Complexes for Chemiluminogenic Bioprobes, *Angew. Chem., Int. Ed.*, 2025, **64**, e202419856.

46 M. Bregnhøj, M. Westberg, B. F. Minaev and P. R. Ogilby, Singlet Oxygen Photophysics in Liquid Solvents: Converging on a Unified Picture, *Acc. Chem. Res.*, 2017, **50**, 1920.

47 Y. Liu, C. Li, Z. Ren, S. Yan and M. R. Bryce, All-organic thermally activated delayed fluorescence materials for organic light-emitting diodes, *Nat. Rev. Mater.*, 2018, **3**, 18020.

48 M. Negi and V. Venkatesh, Near-infrared light-activatable iridium(III) complexes for synergistic photodynamic and photochemotherapy, *Chem. Sci.*, 2025, **16**, 6376–6382.

49 M. Li, J. Xiong, Y. Zhang, L. Yu, L. Yue, C. Yoon, Y. Kim, Y. Zhou, X. Chen, Y. Xu, X. Peng and J. S. Kim, New guidelines and definitions for type I photodynamic therapy, *Chem. Soc. Rev.*, 2025, **54**, 7025–7057.

50 A. K. Yadav, R. Kushwaha, A. A. Mandal, A. Mandal and S. Banerjee, Intracellular Photocatalytic NADH/NAD(P)H Oxidation for Cancer Drug Development, *J. Am. Chem. Soc.*, 2025, **147**, 7161.

51 M. Li, Y. Xu, Z. Pu, T. Xiong, H. Huang, S. Long, S. Son, L. Yu, N. Singh, Y. Tong, J. L. Sessler, X. Peng and J. S. Kim, Photoredox catalysis may be a general mechanism in photodynamic therapy, *Proc. Natl. Acad. Sci. U. S. A.*, 2022, **119**, e2210504119.

52 J. Ruiz, C. Vicente, C. de Haro and D. Bautista, Novel Bis-C, N-Cyclometalated Iridium(III) Thiosemicarbazide Antitumor Complexes: Interactions with Human Serum Albumin and DNA, and Inhibition of Cathepsin B, *Inorg. Chem.*, 2013, **52**, 974.

53 J. L. Perry, M. R. Goldsmith, T. R. Williams, K. P. Radack, T. Christensen, J. Gorham, M. A. Pasquinelli, E. J. Toone, D. N. Beratan and J. D. Simon, Binding of Warfarin Influences the Acid-Base Equilibrium of H242 in Sudlow Site I of Human Serum Albumin, *Photochem. Photobiol.*, 2006, **82**, 1365.

54 L. de C. Bertozo, M. Maszota-Zieleniak, M. Bolean, P. Ciancaglini, S. A. Samsonov and V. F. Ximenes, Binding of fluorescent dansyl amino acids in albumin: When access to the protein cavity is more important than the strength of binding, *Dyes Pigm.*, 2021, **188**, 109195.

55 N. Ibrahim, H. Ibrahim, S. Kim, J.-P. Nallet and F. Nepveu, Interactions between Antimalarial Indolone-N-oxide Derivatives and Human Serum Albumin, *Biomacromolecules*, 2010, **11**, 3341.

56 R. Vinck, O. Dömötör, J. Karges, M. Jakubaszek, J. Seguin, M. Tharaud, V. Guérineau, K. Cariou, N. Mignet, É. A. Enyedy and G. Gasser, In Situ Bioconjugation of a Maleimide-Functionalized Ruthenium-Based Photosensitizer to Albumin for Photodynamic Therapy, *Inorg. Chem.*, 2023, **62**, 15510.

57 H. Sage, R. B. Vernon, S. E. Funk, E. A. Everitt and J. Angello, SPARC, a secreted protein associated with cellular proliferation, inhibits cell spreading in vitro and exhibits Ca+2-dependent binding to the extracellular matrix, *J. Cell Biol.*, 1989, **109**, 341.

58 N. Desai, V. Trieu, B. Damascelli and P. Soon-Shiong, SPARC Expression Correlates with Tumor Response to Albumin-Bound Paclitaxel in Head and Neck Cancer Patients, *Transl. Oncol.*, 2009, **2**, 59.

59 L. Liu, F. Hu, H. Wang, X. Wu, A. S. Eltahan, S. Stanford, N. Bottini, H. Xiao, M. Bottini, W. Guo and X.-J. Liang, Secreted Protein Acidic and Rich in Cysteine Mediated Biomimetic Delivery of Methotrexate by Albumin-Based Nanomedicines for Rheumatoid Arthritis Therapy, *ACS Nano*, 2019, **13**, 5036.

60 X. Li, X. Li, S. Park, S. Wu, Y. Guo, K. T. Nam, N. Kwon, J. Yoon and Q. Hu, Photodynamic and Photothermal therapy via human serum albumin delivery, *Coord. Chem. Rev.*, 2024, **520**, 216142.

61 J. Karges, S. Kuang, F. Maschietto, O. Blacque, I. Ciofini, H. Chao and G. Gasser, Rationally designed ruthenium complexes for 1- and 2-photon photodynamic therapy, *Nat. Commun.*, 2020, **11**, 3262.

